Capturing the mechanosensitivity of cell proliferation in models of epithelium

Kevin Höllring[a], Lovro Nuić[b], Luka Rogić[b], Sara Kaliman[a], Simone Gehrer[a], Florian Rehfeldt[c,d], Maxime Hubert[a,1], and Ana-Sunčana Smith[a,b,1]

[a]PULS Group, Department of Physics, Interdisciplinary Center for Nanostructured Films, FAU Erlangen-Nürnberg, 91058 Erlangen, Germany; [b]Group for Computational Life Sciences, Ruđer Bošković Institute, 10000 Zagreb, Croatia; [c]University of Göttingen, 3rd Institute of Physics-Biophysics, 37077 Göttingen, Germany; [d]University of Bayreuth, Experimental Physics 1, 95440 Bayreuth, Germany

This manuscript was compiled on January 31, 2023

Despite the primary role of cell proliferation in tissue development and homeostatic maintenance, the interplay between cell density, cell mechanoresponse, and cell growth and division is poorly described in theoretical models of tissues. As a consequence, the predictive power of such models is largely undermined, and the lack of systematic statistical and experimental analysis in controlled experiments does not allow to calibrate and validate already existing tools. In this article, we first report an experimental investigation of cell proliferation on all time- and length-scales and quantify the role of cell-cell and cell-matrix interactions. Based on these results, we build a minimal density-driven mean-field model of cell proliferation within 2D epithelia which can account for mechanoresponse and which is based on a separation of cell population into *growing* and *dividing* cells. We show that the model can capture the *in-vitro* experimental results and is further validated by *in-silico* experiments, and we highlight the importance of the separation of time scale and populations in the description of the cell life cycle. Additionally, we show that the mechanoresponse observed in the proliferation patterns is responsible of large-scale density structures across the tissues that we can capture by nonlinear delayed Fisher-Kolmogorov-like equations. This work sets a first building stone in a theoretical description of tissues on long time- and length-scale while accounting for proliferation.

Cell proliferation is the process denoting the increase of the number of cells. In epithelial cell lines, it relies on a tight regulation of the cell cycle which connects *cell growth*, the increase in cell size, to *cell division*, the latter associated with the duplication of DNA and the creation of two daughter cells (1). The time spent by cells growing and dividing is tightly controlled by various biochemical signalling pathways which are well understood and documented in the literature (2, 3). However, recent reports have highlighted the importance of mechanical stresses arising from cell-cell and cell-matrix interactions (4–6), which have been quantified through measures of cell size (7), extracellular stiffness (8–10) and through application of external stresses (7, 11, 12). The ensemble of this work showed that external stresses mainly affect the duration of the growth part of the cell life cycle, leaving the duration of the division part relatively untouched (13, 14). Consequently, increased proliferation is associated with a shorter growing phase, and vice versa. For instance, small cells in tissue sense local higher cell density and therefore larger tissue inner pressure. This leads to a longer lag time in the growing phase which therefore delays proliferation (5).

These results are a clear indication of the mechanoreponsiveness of the growth phase. Indeed, it was demonstrated that it is the growth phase of MDCK cells on polyacrylamide gels that is extended at higher cell density within tissues (15). This result is complemented by a study in which it was shown that the probability for entering the cell cycle increases with the inverse of actual cell size in MDCK and mIMCD-3 cells on glass (7). Thus it remains unclear if the probability for proliferation depends on the cell size alone, or is it affected by the density of the surrounding tissue. Furthermore, while similar trends were found on glass and on softer substrates, current data are not sufficient to show if the probability to proliferate dependent on the stiffness of the underlying matrix.

Another important aspect of cell proliferation is its role in tissue growth, structure, regeneration and homeostasis (16–21). In all these processes, mechanics on the level of a single cell translates into properties of the entire tissue. Hence, one could hypothesize that the mechanosensitivity of the growth phase in cell proliferation affects macroscopic tissue structuring. The latter was itself recently shown to depend on the stiffness of the underlying matrix (22). However, the interplay between the mechanoresponse to matrix stiffness, mechanosensitivity of proliferation and structure formation is a fully open problem. Answering this question, however, necessitates a theoretical approach validated by extensive experimental campaigns.

A large majority of numerical approaches so far, however, assumed cell proliferation to consist of growth only, with the division phase being instantaneous (23–26). Only scarce models treat the proliferation as function of the cell size or density (7, 25), but the applied rules are often phenomenological. These approaches are therefore insufficient to relate the mechanics in the environment, the mechanoresponsiveness of cell proliferation and the tissue compartmentalization.

In this manuscript we address this issue by first characterising experimentally the differences in mechanoresponsive proliferation of cells within tissues grown in different mechanical environments. The obtained dependencies and differences are then captured by a simple model for cell proliferation that explicitly delineates the time for the mechanosensitive cell growth and division phases. We incorporate this model into a continuous description of tissue growth, as well as in dissipative particle dynamics simulations. We show that this comprehensive, yet simple treatment of cell proliferation is essential to reproduce macroscopic tissue structuring, observed

KH developed and validated microscopic model for cell proliferation, the continuous model for tissue growth, and performed the associated comparison with experiments. LN developed the simulation. MH and LR performed the simulations, analyzed the data and together with KH compared the simulations to experiments. SK performed the experiments and analyzed the data with the help of SG, FR, and MH. The article has been written by KH, MH and ASS, with critical insights from all authors. ASS conceived the project, and supervised the experimental and theoretical advances.

The authors declare no conflict of interest.

[1]To whom correspondence should be addressed. E-mail: (MH) maxime.hubert@fau.de, (A-SS) smith@physik.fau.de, asmith@irb.hr

DRAFT

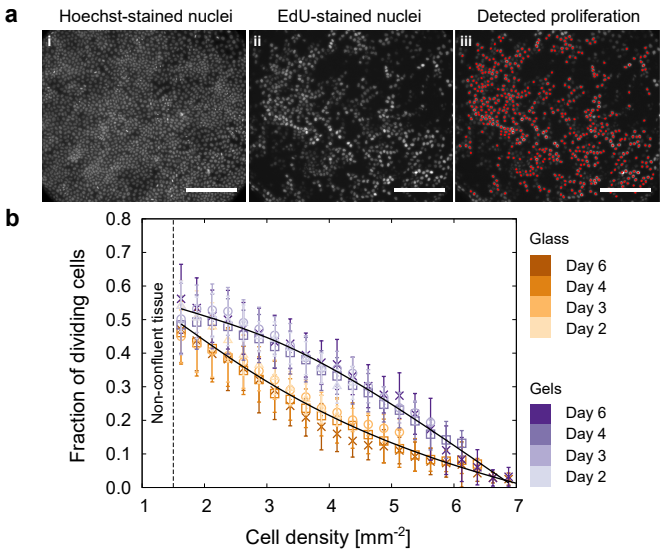

Fig. 1. Division of MDCK-II cells in confluent tissues and its relation to the cell local environment. (a) Illustration of the experimental measure of dividing cells. In these pictures, cells grown for 4 days on 11 kPa gels are both stained with Hoechst (i) and with EdU (ii) after 4 days of unperturbed development. A home-made MATLAB post-treatment software highlights the dividing cells based on their EdU-intensity relative to the background (iii, *methods*). The fraction of dividing cells and the overall cell density are both measured from these images. Scale bar = 200 μm (b) Relation between the fraction of dividing cells $\mathcal{R}$ and the overall cell density for different substrates and different instants of the tissues development. Tissues grown on glass (resp. on 11 kPa gels) are represented in shades of orange (resp. shades of blue). Different symbols account for different time points. The solid lines account for Eqs. (2) and (7), the fitting parameters are summarized in Tab. 1

experimentally on substrates of different stiffness. We believe this work represents a significant step forward in the understanding of the mechanics of tissue growth, which can be now applied in more complex systems.

Influence of the local environment on proliferation in MDCK-II tissues. In order to characterise the probability for proliferation in different mechanical environments, we grow unconstrained model tissues from Madin-Darby Canine Kidney II (MDCK-II) cells in various conditions (see *Methods*, and ref.(22) for details). In short, cells are seeded on glass and 11 kPa PA gels, both coated with collagen I to ensure proper cell adhesion. Confluent monolayers are typically formed 6 hours after seeding, upon which the tissues start to invade the cell-free part of the plane, while densifiying in the middle on the colony (22, 27). The homeostatic state is reached typically 4 days after seeding in the center of the colony with $\rho_h = 6860$ cells/mm^2 (resp. 7280 cells/mm^2) for glass (resp. 11 kPa gels) (22). The moving edge is associated with density gradients which brings the density down to approximately 1 500 cells/mm^2 at the very extremity of the colony. To determine the fraction of dividing cells in maturing tissues, colonies are fixed on day 2,3,4 and 6 after seeding, reaching ultimately radius of 1 cm. Cells are first stained with the Hoechst dye to determine the cell density. Furthermore, EdU staining is used to highlights the S-phase of cell cycle (Fig 1a). To generate sufficient statistics, entire fixed tissues are imaged in epifluorescence using 5× and 20× objectives.

The observable to quantify the proliferation probability of cell within *in-vitro* tissues is the ratio $\mathcal{R}$ of dividing cells and the total number of cells within a region of interest. This variable is mathematically defined as

$$\mathcal{R} = \left\langle \frac{N_d}{N_d + N_g} \right\rangle, \qquad [1]$$

where N refers to the number of cells in a given phase (d or g), and where $\langle \cdot \rangle$ denotes the ensemble average. The size of the region of interest is chosen to be of the order of the density-density correlation length for MDCK cells (28). Hence, the area of interests are fixed to 271×241 μm^2, which accounts for the geometry of the microscopy image. The fraction $\mathcal{R}$ is determined from colonies fixed on different days and substrates with well defined stiffness over the entire density range. This gives rise to a total of 10^4 regions of interest (see Fig. S1), which were consequently binned in cell density windows of 250 cells/mm^2 (Fig. 1b).

Inspection of these results clearly shows that on days 2 and 3 the higher densities are not present (see Fig. S2a), due to the early stages of the maturation. Moreover, at fixed substrate stiffness, data on all days overlap (see Figs. S2b, 2c). This suggests that $\mathcal{R}$ does not depend on the history and spatial positioning of the cell in the central or moving edge compartments of the colony. Indeed, while the spatio-temporal pattern of proliferating cells in the tissue evolves in time and space (22), the results indicate that the spatio-temporal evolution of the cell density is the sole mechanism behind this apparent behavior. As such, $\mathcal{R}$ is only a function of the density in the immediate environment of the dividing cell. As the local cell density increases, the fraction of dividing cells decreases down to almost zero when the homeostatic density is reached on days 4 and 6, a result that is consistent with previous findings (7, 15).

The data also show that the probability of cell proliferation clearly depends on the stiffness of the underlying substrate. Notably, cells grown on glass display a curve with a positive (convex) curvature, while cells grown on gels have a negative (concave) curvature. (Fig. 1b). Such features relate to the observation that cell proliferation is controlled by the mechanical sensing of the environment through integrin-mediated adhesion with the substrate and E-cadherin at the cell membrane (11, 29). The origin of this behaviour remains, however, unclear but is likely to be related to YAP signalling (6).

Microscopic model for cell proliferation. Further insight into the dependence described in the previous section can arise from theoretical considerations. We therefore devise a cell-level model for proliferation. We assume the simplest growth dynamics, i.e. linear in time, for the *growing* part of the proliferation cycle. The transition towards the division phase is cell-area-based. Finally, we assume that mechanoresponse is accounted for by the different numerical values of the parameters of our model.

The observable to quantify the proliferation of cells within *in-vitro* tissues is the local ratio of dividing cells $\mathcal{R}$ within a region of constant local cell density, which which we relate to the duration τ_g and τ_d of the phases as

$$\mathcal{R} = \left\langle \frac{N_d}{N_d + N_g} \right\rangle = \frac{\langle \tau_d \rangle}{\langle \tau_d \rangle + \langle \tau_g \rangle}. \qquad [2]$$

Following reports in the literature (13, 14), we assume that the duration of the division phase is roughly independent of the mechanical conditions within the tissue. On the contrary, we

DRAFT

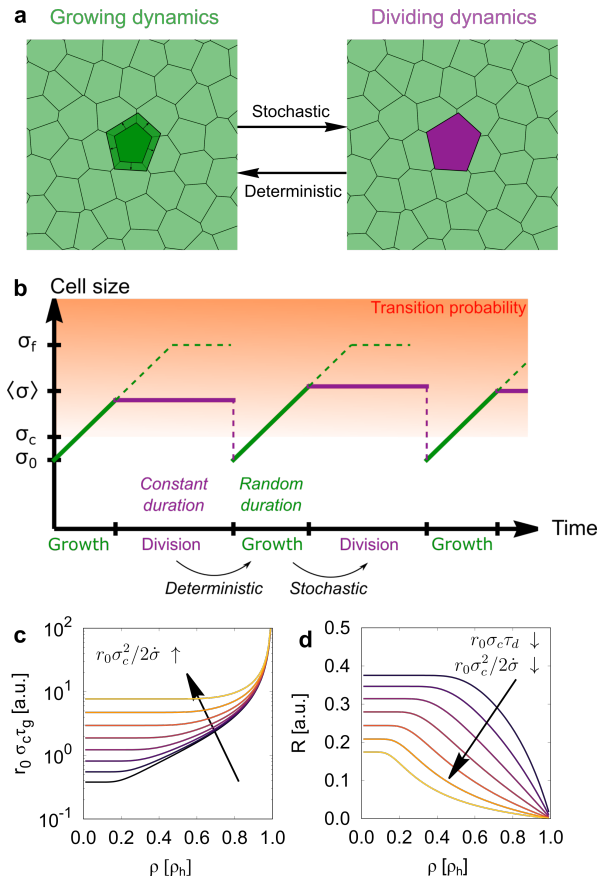

Fig. 2. Microscopic model for cell proliferation (a) Graphs illustrating the different stage of the cell life cycle in our models. The cell grows in size while in the *growth* stage and transits stochastically towards the *division* stage, and remains at constant size for a deterministic amount of time. (b) Illustration of the cell dynamics through time showing the cell size through time, the duration of each phase and the transition probability. (c,d) Mean duration of the growing stage of the cell cycle (c) and fraction of dividing cells (d) for diverse values of the two dimensionless groups $r_0\sigma_c^2/2\dot{\sigma}$ and $r_0\sigma_c\tau_d$. The density is presented as a function of the homeostatic density ρ_h.

assume that the density-dependence of $\mathcal{R}$ (Fig. 1b) is carried only by the duration of the growth phase τ_g (7).

Since cells stochastically enter the division phase of their life cycle (30), we build a stochastic model of cell proliferation based on the increasing size of the cell while in the growth phase: a given cell with size $\sigma(t)$ is located in an environment of homogeneous density ρ, applying as a result an isotropic pressure (Fig. 2a), and setting a target cell size $\sigma_f = 1/\rho$. In our model, in order to keep the local density background homogeneous, only the cell of interest is able to grow as a function of time t, following the formula

$$\sigma(t) = \begin{cases} \sigma_0 + \dot{\sigma}t & \text{if } t < t_c, \\ \sigma_f & \text{if } t > t_c. \end{cases} \quad [3]$$

The parameters $\dot{\sigma}$ and σ_0 represent the growth rate and initial size of the cell respectively. Growth saturates because of pressure building up in the tissue at time t_c.

To relate cell size and stochastic transition towards division, we build an equation for the probability p_g for a cell to be still growing at time t, i.e. that a cell did not divide at time t, as

$$\dot{p}_g(t) = -r\left(\sigma(t)\right) p_g(t). \quad [4]$$

Substrate	$r_0\sigma_c\tau_d$ [-]	$r_0\sigma_c^2/2\dot{\sigma}$ [-]	σ_c^{-1} [cells/mm^2]
11 kPa gels	0.886	0.314	7081
glass	0.359	0.0662	7216

Table 1. Fitting parameters used for comparing Eqs. (2) and (7) to the MDCK-II experiments presented in Figure 1b.

The parameter $r(\sigma)$ is a size-dependent division rate which we define as

$$r(\sigma) = \begin{cases} 0 & \text{if } \sigma < \sigma_c, \\ r_0(\sigma - \sigma_c) & \text{if } \sigma > \sigma_c. \end{cases} \quad [5]$$

The parameter σ_c is the lowest size for which division can occur, therefore setting the homeostatic density $\rho_h = \sigma_c^{-1}$ and is expected to obey the relation $\sigma_c < \sigma_f$ for division to be possible (Fig. 2b). The parameter r_0 accounts for the increasing probability of division as the cell size σ increases. Equations (4) and (5) together give access to the average time τ_g, writing

$$\tau_g = \int_0^\infty p(t)\,dt = \int_0^\infty \exp\left(-\int_0^t r(\sigma(u))\,du\right) dt, \quad [6]$$

and leading to

$$\tau_g = \frac{\sigma_c}{2\dot{\sigma}} + \sqrt{\frac{\pi}{2r_0\dot{\sigma}}}\,\mathrm{erf}\left(\frac{r(\sigma_f)}{\sqrt{2r_0\dot{\sigma}}}\right) + \frac{\exp\left(-\frac{r(\sigma_f)^2}{2r_0\dot{\sigma}}\right)}{r(\sigma_f)}. \quad [7]$$

Details for this computation are provided in the SI.

The average time spent on the *growing* phase is seen to increase monotonously as the density increases (Fig. 2c). Importantly, this time diverges toward infinity as the cell density increases towards the homeostatic density ρ_h. The overall shape of the curve as well as the time spent in the *growing* phase at very low density, i.e. $\rho \to 0$ largely depends on the value of the parameters r_0 and $\dot{\sigma}$, through the dimensionless group $r_0\sigma_c^2/2\dot{\sigma}$.

The formula for τ_g, i.e. (Eq. (7)), gives access to the fraction of dividing cells $\mathcal{R}$ once a value is given to the parameter τ_d. Given the evolution of τ_g, the ratio $\mathcal{R}$ decreases monotonously towards zero at the homeostatic density ρ_h (Fig. 2d), corresponding to the contact inhibition of proliferation which characterize the homeostatic state (6). Moreover, the shape of the curve is seen to change drastically depending on the combination of values of the three parameters r_0, $\dot{\sigma}$, and τ_d. More precisely, the shape of the curve is controlled by the two dimensionless groups $r_0\sigma_c^2/2\dot{\sigma}$ and $r_0\sigma_c\tau_d$.

Therefore, mechanoresponse in this model is captured effectively by the combination of these two values. One can fit Eq. (2) onto the experimental fraction of dividing cells (Fig.1(b)) to obtain more insights in cell mechanoresponse and its influence on proliferation. The fitting parameters are provided in Tab. 1 for comparison. Fitted values indicate that proliferation of cells on gel corresponds to relatively large values of $r_0\sigma_c\tau_d$ and $r_0\sigma_c^2/2\dot{\sigma}$ with respect to the case on glass. Addressing which of the three parameters play the main role in mechanoresponse would require precise time analysis on a single cell level within the tissue, a information not yet available in the literature. However one can provide more insights on these questions by relying on some assumptions and a careful analysis of of Eqs. (2) and (7).

DRAFT

By fitting the theory, one sees the homeostatic density $\rho = \sigma_c^{-1}$ has a similar value for both substrates, as already observed in a previous publication (22). Moreover, following the assumption that the growing phase is the sole carrier of mechanoresponse, one can set the duration of the division phase τ_d to a given value. As a result, one must consider the joined role of $\dot{\sigma}$ and r_0 to mimic the overall behavior of $\mathcal{R}$ (Fig. (1b). A careful analysis (see SI) shows that the curvature is highly sensitive to the value of r_0. More specifically, under these assumption, large r_0 promote gel-like results. To compensate for the change of fraction of dividing cells at low density, one also need to change $\dot{\sigma}$. More precisely, larger $\dot{\sigma}$ comes together with larger stiffness, a result corroborated by analysis on rapidly spreading MCF-7 at the single cell level when grown on PAAm gels for a fixed duration of 12h (31).

From a theoretical point of view, our cell-level model aligns with the description of Smith and Martin of single cell proliferation (30, 32), which is use profusely in the case of immune cells (33), but here giving this model a mechanoresponsive twist. Indeed, given Eq.(4), one can derive the statistics of time spent in the growth phase (see SI for details), the so-called α-curve (32), and relate such distribution to the parameters of our mechanoresponsive model at the cell-level. Moreover, one can show (see SI) that Eqs. (3,4,5) constitute a minimal model in order to capture the shape of the experimental $\mathcal{R}$-curve and the shape of the α-curve (32). In other words, simpler division protocols, such as a deterministic cell division above a given threshold (23–26, 34, 35) or a constant probability to enter division above a given threshold (36), do not reproduce the features of the experiments (Fig. 1b) (see SI).

Capturing the mechanoresponse of proliferation in DPD simulations. As an additional mean of verification of our microscopic model, we now use Dissipative Particle Dynamics (DPD) simulations. This technique has been used in the context of epithelial dynamics for more than a decade (24–26, 34, 35, 37–40). In such simulations, each cell is only made of two points which are sources and targets of all the forces present in the tissue. Modelling cells with two points gives the possibility to define a cell inner force $F_g = B/(l + r^\star)^2$, which induces cell growth by increasing the distance l between these two building particles (Fig.3a, see SI). In this formula, B is an intensity and $r^\star$ an offset to avoid numerical divergence. Following the ingredients used in the microscopic model, we define the probability to enter the division phase as

$$\mathcal{P}_{\text{div}} = (l - R_{c1})/(R_{c2} - R_{c1}), \qquad [8]$$

where R_{c1} and R_{c2} are two size thresholds. This probability is evaluated at each time step of the simulation. While in the *division* phase, we cancel F_g and introduce instead a force $F_d = K_d(l - l^\star)$ to keep the size of the cells constant, where K_d is a large stiffness and $l^\star$ is the cell size when entering the division phase. The cell remains in the division phase for a constant duration τ_d. Following this division, two daughters cells are produced in their growth phase with $l = l_0$ the initial particles distance.

Mimicking the previously-described experiments, we perform simulations of expanding freely monolayers in two dimensions. We measure the fraction of dividing cells in regions of constant cell density (Fig. 3b). Such regions of constant density are sampled at various positions and at various instants of the tissue development. Similarly to the experimental results, we measure a fraction of dividing cells which decreases monotonously from a constant value at low density towards zero at the homeostatic density (Fig. 3c). Again, the curve obtained is time- and space-independent as all curves overlap onto a single master curve. Playing both on the value of R_{c2} and τ_d, one can tune the curvature of the $\mathcal{R}(\rho)$ (Fig. 3c). Increasing the value of R_{c2} and τ_d leads to an overall curvature change from negative to positive. This effect can be understood by computing the rate r_0 in the case of the simulation (see SI), whose value is directly related to the value of R_{c2}.

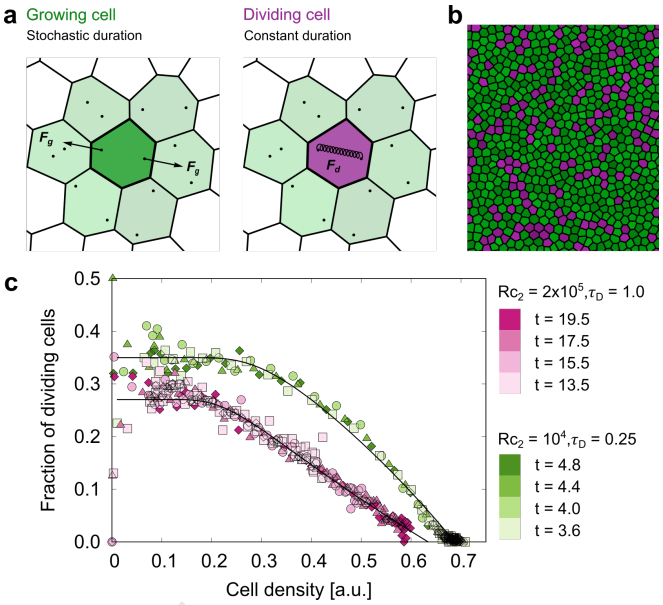

Fig. 3. Quantification of proliferation in numerical simulations of expanding epithelia. (a) Schematics illustrating the inner forces within the cells in the DPD simulations depending on their state, i.e. *growing* or *dividing*. (b) Snapshot illustrating the dividing cells within the expanding tissue. *Growing* cells are represented with shades of green while *dividing* cells are represented with shades of purple. (c) Fraction of dividing cells in the tissue as a function of the local density for two simulations with different values of R_{c2} and τ_d as indicated in the legend. Different instants are considered as highlighted by the different shades of green and pink. All other parameters used in the simulations are indicated in Ref. (22).

Finally, the microscopic theory of proliferation developed in the previous section is confronted to the simulations. We fit Eq. (2) on the simulations performed for different values of R_{c2} and τ_d. Similarly to the experiments, the microscopic model of cell proliferation captures precisely the numerical behaviour (Fig. 3c). The fitting parameters, expressed in terms of dimensionless groups, are provided in Tab. 2 and shows a similar trends as with the experiments.

$\mathbf{R_{c2}}$ **[s.u.]**	τ_d [s.u.]	$r_0\sigma_c\tau_d$ [-]	$r_0\sigma_c^2/2\dot{\sigma}$ [-]	σ_c^{-1} [s.u.]
$\mathbf{10^4}$	**1.0**	0.789	0.716	0.69
$\mathbf{2 \times 10^5}$	**0.25**	0.365	0.414	0.63

Table 2. Fitting parameters used for comparing Eqs. (2) and (7) to the DPD simulations in Figure 3c.

Dissipative particles dynamics simulations have already been successfully used in proliferation-related problems in the case of spheroids submitted to isotropic osmotic pressure (25, 26), albeit with a deterministic division above a given size threshold. While it has been shown previously that DPD sim-

DRAFT

ulation can reproduce the role of external applied pressure as a mean of limitation of cell proliferation, by restraining and even preventing cell growth, the simplicity of such division protocol does not allow for capture of mechanoresponsive properties. Indeed, as shown on Fig. 3 and as demonstrated mathematically in the SI, the reproduction in numerical simulations of mechanoresponsive proliferation relies on the inclusion of different rate of cell division with the cell size (namely different r_0). Such results align with our previous assumption regarding the experiments that mechanoresponse, and consequently the different curvature of $\mathcal{R}$ with the density, is mainly carried by the parameter r_0.

Macroscopic structure of the tissue. Proliferation can be a source of stress and tension within the monolayer, which as a result can affect its large scale structure (41). Given the very different curves corresponding to different mechanoresponse (Fig. 1b and Fig. 3c), one can therefore expect different macroscale compartments in the corresponding tissues. Indeed, the expansion and maturation of the tissue on glass with tissues on gel show two different outcomes (Fig. 4(a,b)). For both substrates, the tissues display a similar behaviour 2 days after seeding. In this case, proliferation is roughly proportional to the cell density. Six days after sending however, density and proliferation become anti-correlated, and the tissues display different macroscopic compartments as describe in a previous study (22). The most important difference comes from the H_p, an homeostatic state which is only proliferation-inhibited, and only present on 11 kPa gels.

To address theoretically the role of mechanoresponse in the compartmentalization observed experimentally, we need to integrate the relation between proliferation and local cell density over time and space. To reach this goal, we build on the well-known Fisher-Kolmogorov (FK) equation (37, 42, 43). In this context, the expansion of the tissue is described through a diffusion-like process with efficiency D and the cell proliferation is described through a logistic-like growth process with efficiency β. In our case, we introduce two populations ρ_g and ρ_d, and non-linearities through a power law with exponent c which will account for effective mechanoreponse (full discussion in the SI). The latter controls the curvature of $\mathcal{R}(\rho)$ through a single parameter and therefore accounts for the simplest mean of inclusion of mechanoresponsiveness (see SI). The set of corresponding equations is

$$\frac{\partial \rho_g}{\partial t} = D\Delta\rho_g - \beta(\rho_h - \rho)^c \rho_g + 2\beta(\rho_h - \rho(\tau))^c \rho_g(\tau), \quad [9]$$

$$\frac{\partial \rho_d}{\partial t} = \beta(\rho_h - \rho)^c \rho_g - \beta(\rho_h - \rho(\tau))^c \rho_g(\tau), \quad [10]$$

where $\tau = t - \tau_d$, which comes from the time spent in the division phase, leads to delayed terms in the equations. The total density $\rho = \rho_g + \rho_d$ is given by the sum of the two above equations leading to

$$\partial_t \rho = D\Delta\rho_g + \beta(\rho_h - \rho(\tau))^c \rho_g(\tau). \quad [11]$$

We refer to the equations above as Delayed nonlinear Fisher-Kolmorogov-like (DFK) equations. Specifically, the case $c = 1$ and $\tau_d = 0$ transforms Eq. (11) to the usual FK equation (37).

We numerically solve these equations with a home-made delayed differential equation solver (see *methods*) and investigate the sole influence of c on the final structure of the tissue (Fig. 4(c,d)). Similarly to the experiments, at the early stages of development, the proliferation of cells correlates strongly with the cell density and little differences are observed between the glass-like ($c = 2$) and gel-like ($c = 0.5$) situations. With time, as density is increasing in the bulk and the tissue is expanding, the bulk of the tissue becomes proliferation- and locomotion-inhibited. Cell proliferation only occurs at the tissue outer edge. Interestingly, the differences that can be observed in the two cases $c = 2$ and $c = 0.5$ match the ones that occur in experiments. Indeed, the gel-like case ($c = 0.5$) has a H_p compartment (22). This feature is not reproduced in the glass-like case ($c = 2$) where the density instead drops monotonously and slowly (with respect to the case $c = 0.5$) towards zero. From a physical perspective, the compartment H_p can be understood by the existence of the delay τ. Since the production of two daughter cells happens after a time τ_d after the mother has been allowed to enter the division stage by sensing the local density, the local density can overshoot beyond the homeostatic value. Density-overshoot are more therefore likely to happen on gels-like situation ($c < 1$) as the probability to divide close to homeostasis is still high with respect to glass-like dynamics ($c > 1$).

Such differences in macroscopic structures can also be reproduced with DPD simulations by directly affecting the rate r_0 via the parameter R_{c2} (see Eqs. (5), (8), and SI). Indeed, the case of small R_{c2} ($R_{c2} = 10^2$, see Fig. 4e) leads to an overshoot of density at the outer edge where proliferation is contact-inhibited, therefore mimicking the behaviour of MDCK-II tissues on gels. On the contrary, the case of large R_{c2} leads to a slowly decreasing density profiles mimicking the dynamics on collagen-I-coated glass. As already described previously, a change of R_{c2} influences the value of r_0 (see SI) and consequently the dimensionless groups $r_0\sigma_c^2/2\dot{\sigma}$ and $r_0\sigma_c\tau_d$.

Deviations from the usual FK formalism have already been observed experimentally by Metzner *et al* (42) using HT1080 fibrosarcoma cells and MCF7 mammary gland adenoscarcinoma cells. In their article, the deviations appeared in the form of non-linear contributions to the proliferation term, which are captured through complex empirical fitted functions. On the contrary, our DFK formalism allow to investigate non-linear contributions to proliferation through a minimalistic approach, namely the variation of the exponent c which tunes to responsiveness of cell to enter division while being close to homeostasis and the curvature of $\mathcal{R}(\rho)$. As we have seen, coupled to the existence of a delay τ such a variation of c can create new density profiles and tissue growth.

While the exponent c relates to mechanoresponse, no direct correlation can be made with the microscopic model presented earlier in this manuscript. Indeed, the microscopic model predicts a polynomial behaviour for the $\mathcal{R}$ function around the homeostatic density (see SI). However, by definition, the DFK model produces a power-law behavior around the homeostatic density which is controlled by a single parameter: the exponent c. As such, it is not possible to relate both model directly. A more quantitative agreement would involve a significant rework of the DFK equations, by crafting a more complex proliferation term instead of the actual non-linear logistic growth term. With such complexity would come several parameters which would blur the role of the curvature of the $\mathcal{R}$ function and its consequence on large scale structure.

DRAFT

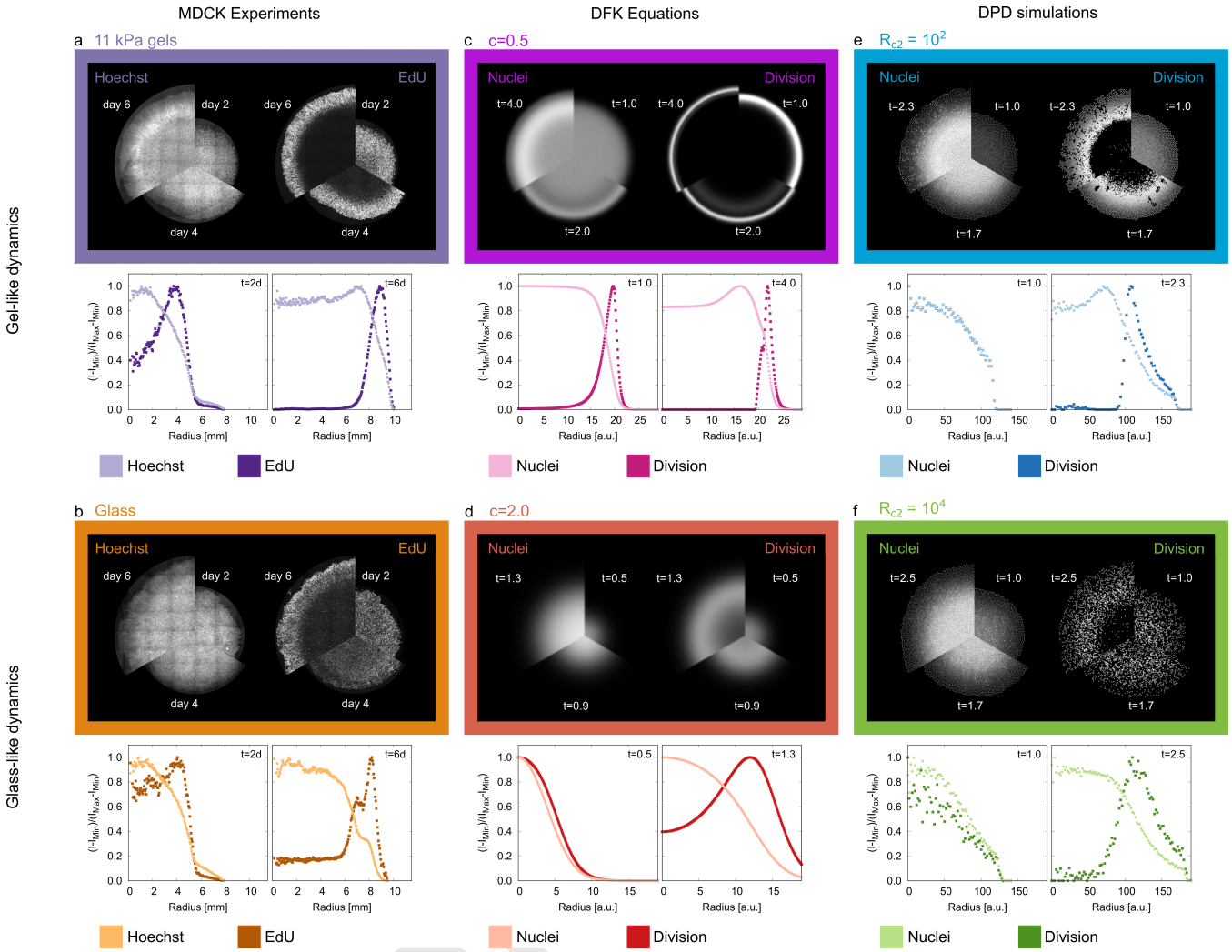

Fig. 4. Macroscopic structure of expanding tissues and their relation to mechanoresponsive proliferation. (a,b) Space-time evolution of the Hoechst intensity and EdU intensity across the tissues during its unconstrained expansion. The light intensity for both the Hoechst and EdU directly relates to the cell density. Normalized radial intensity profiles at day 2 and day 6 are presented for quantitative comparison. (c,d) Space-time evolution of the local nuclei density, i.e. $\rho_g + \rho_d$, and proliferating cell density, i.e. ρ_d, obtained from solving Eqs. (9) and (10). Mimicking the experimental results is possible by changing the parameter c. Other parameters are kept constant. Normalized profiles for each signal are also provided for two different instants. (e,f) Space-time evolution of cell density and proliferating cell density as obtained from DPD simulations. Mimicking the experimental results is possible by changing the parameter R_{c2}. Other parameters are kept constant. Normalized profiles for each signal are also provided for two different instants.

It must finally be stated that the DFK formalism aims at highlighting the role of proliferation and associated mechanotransduction in the growth of tissues and subsequent compartmentalization. Other mechanisms and their own associated mechanotransduction, such as collective migration and associated durotaxis (44), are not accounted for. Therefore, a complete picture of the relevant players in tissue maturation can only come with a more in-depth description of such mechanoresponsive contributions to development.

Discussion

Beyond the experiments discussed in this article, our theoretical framework can shed some light in recent experimental reports in the literature. For instance, it has been shown that stretching a dense tissue along a single axis (7) or along the two axis (11) leads to a burst of division events, even reactivating proliferating dynamics despite having been at homeostasis (7). Such results can be easily understood under the light of our microscopic model, where stretching can simply bring the cell in the regime where $p_g \neq 0$ (see Eq. (4)). The time upon which the burst of dividing cells reach its maximum could also be predicted by our theory based on the stretching amplitude. Naturally, the opposite experiment, namely compression (25, 26, 45), could lead to an arrest of proliferation by bringing the cells in the regime where $p_g = 0$ depending on the compression amplitude. Predictions for such an experiments can also be done based on our theory.

Our model can also help bring insights into debated experiments. For instance, Kafi *et al* grew HeLa (human cervical) and HEK293T (human embryonic kidney) cells on functionalized nano-dot, nano-rods and nano-pillars (46). They measured increased proliferation in functionalized surface with respect to control, and also increased proliferation for taller nano-structures. While the authors explained the role of functionalization by stating that it properly matched receptor-

mediated binding with integrin receptors on the cell membrane, the role of the length of the nano-structures was not understood. Through our model, and knowing that the length of nano-pillar is inversely proportional to their stiffness, one could hypothesize that the enhanced proliferation actually relate to mechanotransduction, an assumption strengthened by the observation of larger cell area on taller nano-structures. Similar influence of nano-structure on proliferation are observed when changing the diameter of the nanopillars (47).

Finally, we believe that our study will shed a new light on the interaction of proliferation and maintenance of homeostasis in various epithelia. Indeed, various skin diseases for example alter the mechanical properties of the basal membrane which alter deeply the proliferation behavior of cells (48, 49), which increases for larger stiffness.

Conclusions

In conclusion, we reported a first systematic experimental investigation of cell proliferation in tissues on all time- and length-scales, its relation to the local cell density and considered the influence of the mechanical properties of the immediate environment. We have shown that the the fraction of proliferating cells only relates to the local density and the shape of this relation is dictated by mechanoresponse. We presented a minimal microscopic mean-field model of cell proliferation in tissues. This model only takes into consideration the mechanical properties of the local environment of the cell and split in two populations the different stages of the cell life cycle. The model has been successfully compared with DPD simulations and experiments performed with MDCK-II cells. In both cases, the division dynamics of cells has been accurately linked to the local cell density which measures indirectly the pressure applied to cells and also captures the mechanoresponse observed in cell proliferation. Having understood the influence of density on proliferation, we focused on understanding the influence of proliferation and mechanoresponse on large scale density structures. For this purpose, we developed a set of nonlinear delayed Fisher-Kolmogorov-like equations which can incorporate mechanosensing. We have shown that the density profile across the tissue and its time evolution can be deeply affected by mechanoresponsive cell proliferation. This work opens a new perspective on cell proliferation and on the theoretical description of developing epithelial tissues.

In the near future, we not only hope this new detailed description will provide a better understanding on the growth and development of epithelial tissues, but also provide new perspectives of investigations of epithelia-related diseases and their eventual relations to alteration of the stiffness of the extracellular matrix.

Methods

Numerical resolution of the DFK equations. To obtain the numerical solution of the DFK equations (Eqs. (9) and (10)), we implemented a custom python script to compute the time evolution of the density distributions $\rho_{g,d}$ for a given set of parameters (ρ_h, D, τ_d, β, c) by solving a radially symmetric tissue with $\rho(\vec{r},t) = \rho(r,t)$.

Using the polar representation of the Laplace operator together with $\partial_\phi \rho_{g,d} = 0$, i.e. an homogeneous tissue along the azimuthal direction, the radial components of the DFK equations are given by Eqs. (12) and (13). The equations are integrated on an interval $r \in [0, R]$ with reflecting boundary conditions at the origin, i.e. $\partial_r \rho_{g,d}(r = 0, t) = 0, \forall t$, and absorbing boundary conditions at the outer boundary, i.e. $\rho_{g,d}(r = R, t) = 0$. As initial conditions, we assume a static density distribution with no proliferation, namely

$$\rho_g(r, t \leq 0) = \begin{cases} \rho_{\text{init}} & \text{if } r \leq r_{\text{init}}, \\ 0 & \text{else,} \end{cases} \quad [14]$$

$$\rho_d(r, t \leq 0) = 0. \quad [15]$$

Spatial discretization is performed with a discrete step of Δr leading to discrete positions $r_i = i\,\Delta r$. The numerical derivatives are calculated by central differences, i.e. $\partial_r f(r_i) = (f(r_{i+1}) - f(r_{i-1}))/(2\Delta r)$, while the Laplace operator is implemented as the usual central stencil, i.e. $\Delta_r f(r_i) = (f(r_{i+1}) - 2f(r_i) + f(r_{i-1}))/(\Delta r)^2$.

The numerical solution of the time evolution of $\rho_{g,s}$ is obtained via a custom SciPy-based python module *ddesolver* (https://github.com/Reshief/ddesolver), which is a modification of the python module *ddeint* (https://github.com/Zulko/ddeint) with higher numerical accuracy thanks to a Runge-Kutta 4/5 integration steps and time-step rescaling. To account for the delayed term of the DFK, a history of states for simulated times $t \geq 0$ is kept. This history is looked into during integration, and linear interpolation is used between subsequent simulated time steps. Such history repository are implemented for both densities ρ_g and ρ_d independently. The simulation is then carried out for a total time $T > 0$ with a time discretization step of a maximum of Δt in arbitrary units.

The values of simulation parameters are summarized into Tab. 3. The data for $R(\rho)$ is obtained by time-averaging and binning of the ratios ρ_s/ρ as a function of ρ at all positions with $\rho_0 \geq \rho \geq 0.01$ with 40 equidistant ρ-bins on the interval $[0, \rho_0]$.

Parameter	Values
D	0.5, 1.0, 2.0, 3.0
β	1.0, 2.0, 3.0
c	0.25, 0.5, 1.0, 1.5, 2.0
τ_d	0.25, 0.5, 1, 2, 3, 4, 5
R	100
r_{init}	5
ρ_{init}	1.0
ρ_h	1.0
Δt	0.01
t	100
Δr	0.25

Table 3. Values of parameters chosen for the numerical integration of the DFK system of equations.

Dissipative Particle Dynamics simulations. Dissipative Particle Dynamics (DPD) simulations are an agent-based class of algorithm that have been used successfully in biophysics and which are highly adaptive as it can be seen from the large number of applications in different scientific fields.

In the context of epithelial growth, each cell within the tissue is approximated by two points that are sources and targets of all forces in the system (see 3a). All forces, viscous or deriving from a potential, are pairwise implying that momentum is conserved in the system. A complete list and

DRAFT

$$\partial_t \rho_g(r,t) = D\left(\partial_r^2 + \frac{1}{r}\partial_r\right)\rho_g(r,t) - \beta\left(1-\frac{\rho(r,t)}{\rho_h}\right)^c \rho_g(r,t) + 2\beta\left(1-\frac{\rho(r,\tau)}{\rho_h}\right)^c \rho_g(r,\tau)\Big|_{\tau=t-\tau_d}, \quad [12]$$

$$\partial_t \rho_d(r,t) = \beta\left(1-\frac{\rho(r,t)}{\rho_h}\right)^c \rho_g(r,t) - \beta\left(1-\frac{\rho(r,\tau)}{\rho_h}\right)^c \rho_g(r,\tau)\Big|_{\tau=t-\tau_d}. \quad [13]$$

mathematical definition of the forces is provided in a previous publication (22). Cells interact with their neighbours via a Lenard-Jones-like potential, allowing for stiff short-range repulsion and soft long-range attraction. Cells are submitted to a viscous drag proportional to the cell velocity measured with respect to the background. A second drag is applied and is proportional to the relative speed between neighbouring cells, opposing the relative motion. Within a single cell, during the growth phase, the two building particles repel through a repulsive force mimicking an inner pressure ($\vec{F}_g$), necessary for cell growth and cell division. While in the division phase, the building particles are kept at a constant distance by a stiff harmonic force ($\vec{F}_d$). Also, a random force of uniform angular distribution and normally distributed intensity is applied to all particles and accounts for passive fluctuations in the tissue.

The simulations also account for active ingredients. Cell division is a stochastic process and is made of two phases. The first phase, named the "growth phase", is characterized by a pressure built up within the cells, increasing the distance $l = |\vec{r}_{j,1} - \vec{r}_{j,2}|$ between the two building particles {1,2} of cell j. As this distance crosses a threshold R_{c1}, the cell as a non-zero probability to enter the second phase or "division phase". The probability is given by

$$\mathcal{P}(l) = \frac{l - R_{c1}}{R_{c2} - R_{c1}}, \quad [16]$$

where R_{c2} is a second threshold above which the probability is equal to one. Once in the *division* phase, the inner pressure disappears and instead the cell distance is kept at the value it has when entering the *division* phase. While the duration of the growth phase is stochastic and depends on the parameters of the simulations, the duration of the division phase is a parameter and is set to a fixed value.

The final active ingredient of the simulation links cell position and cell shape. The cell shape is obtained by Voronoi Tessellation based on the average distance between the two building points, mimicking the cell nucleus in the simulation. The cell motility is obtained by applying a limited Lloyd optimization step to the cell nuclei position. Specifically, if $d = |\vec{r}_{nuc} - \vec{r}_{cell}|$ where $\vec{r}_{nuc}$ and $\vec{r}_{cell}$ are the nuclei and cell centres respectively, then the nuclei is moved by a distance λd towards the cell center where λ is the amplitude of the Lloyd optimization step.

Cell Culture and gels preparation. The preparation of gels and the culture of cells follow the procedure used in a previous publication of our group (22).

MDCK-II cells were obtained from ECACC, UK (Cat #00062107, RRID:CVCL_0424) and cultured in MEM Earle's medium (#F0325, Biochrom) supplemented with 5% fetal bovine serum (FBS, #F0804, Sigma-Aldrich), 2mM L-glutamine (#G7513, Sigma-Aldrich), and 1% penicillin & streptomycin (#15070-063, Gibco, LifeTechnologies) at 37°C and 5% CO_2. Cells were passaged every two or three days before reaching 80% confluence.

Elastic polyacrylamide (PA) gels were prepared as follow. Appropriate mixtures of acrylamide (40% solution, BioRad) and bis-acrylamide (2% solution, BioRad) were polymerized by addition of 0.1%(v/v) N,N,N,N tetramethylethylenediamine (TEMED) and 1%(v/v) ammonium persulfate (APS) for 60 minutes at RT on plasma cleaned glass cover slips (No.1, 25mm ∅, VWR) that were pre-treated with 3-aminoproyltriethoxysiliane (APTES, Sigma-Aldrich) for 15 minutes and incubated with a 0.5% solution of glutaraldehyde in PBS (Sigma Aldrich) for 30 minutes. For quality control reasons, we used the stock solutions not longer than 3 months stored at 4°C and protected from light and ideally prepared as many samples from the same batch as needed.

After polymerization the PA gels were washed extensively with PBS and subsequently coated with Collagen-I (BD Biosciences) at 0.02 mg/mL in a 50 mM HEPES buffer using the bi-functional cross-linker Sulfo-SANPAH (Pierce, Thermo Scientific) activated for 10 minutes with UV light (365 nm). Here, we use the conditions optimized in (50), at which the concentration of collagen on the surface is fully saturated, to avoid deviations in available collagen density, and to make sure that adhesive properties of the surfaces are identical in all cases.

Imaging. Tissues were fixed using a 10% solution of formaldehyde (formaldehyde, #47608, Sigma-Aldrich) in PBS for 5 minutes, and the cells were permeabilised for 10 minutes using a 0.5% solution of Triton X 100 (Carl Roth). After washing with PBS, samples were blocked using 3% BSA (#A9418, Sigma-Aldrich) in PBS for 30 minutes at RT, which preceded another Triton X 100 treatment of 5 minutes at RT, followed by 3 washing steps with PBS.

Epifluorescence microscopy images were acquired on an inverted microscope (Zeiss Cell Obsever Z1) using 5× and N-Achroplan 20× objectives, using AxioCam M3 and AxioVision software package (all Zeiss). Confocal microscopy was performed on a Leica LSM SP5 laser-scanning microscope equipped with a white light laser and a 63× and a 100× oil immersion objective yielding fields of view of (246 μm × 245 μm) and 100× (155 μm × 155 μm) respectively. The step size in the z-direction was kept constant at 0.25 μm. All tissues grown in one series were fixed and stained simultaneously and imaged consecutively without changing the microscope settings.

Density and proliferation analysis. To quantify density and proliferation, we first segmented Hoechst-stained-nuclei picture using MATLAB. From the number of the nuclei center of mass we can evaluate the cell density, and from the position of the center of mass, we can evaluate the cell proliferation using the EdU-stained-nuclei pictures.

Firstly, 5% of the original 3.2×2.7 mm^2-image is removed at the edge because of the overlap between adjacent images

DRAFT

in the overall picture of the cluster. Following that step, the reduced images are divided in 108 segments with size 271×241 μm^2 to avoid segmentation error due to a single thresholding parameter being applied to the whole image. On each of the 108 sub-pictures, the Otsu method is used to determine the optimal thresholding parameter. From the binary images resulting from segmentation, a distance-transform is applied and followed by a standard watershed algorithm. The final result is a segmentation of nuclei which allows to extract their center of mass. The cell density is then evaluated by taking the number of nuclei divided by the area of the reduced picture. In average, such a procedure provides in-between 130 and 480 cells with area varying from 1500 cells/mm^2 up to 7000 cells/mm^2.

Secondly, knowing the outline of the nuclei from the Hoechst picture, one can evaluate the EdU intensity on the corresponding EdU picture. If the EdU-intensity at the nucleus position is higher than 95% of the average EdU-intensity of the image segment, the cell is tested positive for proliferation. Knowing the number of dividing cells in the image segment and the total number of cells in the corresponding Hoechst image, one has access to the ratio of proliferating cells.

ACKNOWLEDGMENTS. This work was in part supported by the German Research Foundation projects RTG 1962 (ASS, SG), RTG 2415 (ASS, MH, KH), SFB 755 project B08 (FR), the ERC StG 337 MembranesAct (ASS, SK, LN), and by the Emerging Fields Initiative "BigThera", which was partly supported by the Staedler Foundation (ASS).

1. Lloyd AC (2013) The Regulation of Cell Size. *Cell* 154(6):1194–1205.
2. Saxton RA, Sabatini DM (2017) mTOR Signaling in Growth, Metabolism, and Disease. *Cell* 168(6):960–976.
3. Tyson JJ, Novák B (2022) Time-keeping and decision-making in the cell cycle. *Interface Focus* 12(4).
4. Godard BG, Heisenberg CP (2019) Cell division and tissue mechanics. *Current Opinion in Cell Biology* 60(i):114–120.
5. Gupta VK, Chaudhuri O (2022) Mechanical regulation of cell-cycle progression and division. *Trends in Cell Biology* 32(9):773–785.
6. Aragona M, et al. (2013) A mechanical checkpoint controls multicellular growth through YAP/TAZ regulation by actin-processing factors. *Cell* 154(5):1047–1059.
7. Streichan SJ, Hoerner CR, Schneidt T, Holzer D, Hufnagel L (2014) Spatial constraints control cell proliferation in tissues. *Proceedings of the National Academy of Sciences* 111(15):5586–5591.
8. Kim JH, Asthagiri AR (2011) Matrix stiffening sensitizes epithelial cells to EGF and enables the loss of contact inhibition of proliferation. *Journal of Cell Science* 124(8):1280–1287.
9. Janmey PA, Fletcher DA, Reinhart-King CA (2020) Stiffness Sensing by Cells. *Physiological Reviews* 100(2):695–724.
10. Uroz M, et al. (2018) Regulation of cell cycle progression by cell–cell and cell–matrix forces. *Nature Cell Biology* 20(6):646–654.
11. Benham-Pyle BW, Pruitt BL, Nelson WJ (2015) Mechanical strain induces E-cadherin–dependent Yap1 and β-catenin activation to drive cell cycle entry. *Science* 348(6238):1024–1027.
12. Nestor-Bergmann A, et al. (2019) Decoupling the Roles of Cell Shape and Mechanical Stress in Orienting and Cueing Epithelial Mitosis. *Cell Reports* 26(8):2088–2100.e4.
13. Pardee AB (1989) G1 events and regulation of cell proliferation. *Science* 246(4930):603–608.
14. Fan Y, Meyer T (2021) Molecular control of cell density-mediated exit to quiescence. *Cell Reports* 36(4):109436.
15. Donker L, et al. (2022) A mechanical G2 checkpoint controls epithelial cell division through E-cadherin-mediated regulation of Wee1-Cdk1. *Cell Reports* 41(2):111475.
16. Wyatt TPJ, et al. (2015) Emergence of homeostatic epithelial packing and stress dissipation through divisions oriented along the long cell axis. *Proceedings of the National Academy of Sciences* 112(18):5726–5731.
17. Dye NA, et al. (2017) Cell dynamics underlying oriented growth of the Drosophila wing imaginal disc. *Development* 144(23):4406–4421.
18. Ladan MK, Ziherl P, Šiber A (2019) Topology of dividing planar tilings: Mitosis and order in epithelial tissues. *Physical Review E* 100(1):012410.
19. Wensink HH, et al. (2012) Meso-scale turbulence in living fluids. *Proceedings of the National Academy of Sciences of the United States of America* 109(36):14308–14313.
20. Rossen NS, Tarp JM, Mathiesen J, Jensen MH, Oddershede LB (2014) Long-range ordered vorticity patterns in living tissue induced by cell division. *Nature Communications* 5(May):1–7.
21. Doostmohammadi A, et al. (2015) Celebrating Soft Matter's 10th Anniversary: Cell division: a source of active stress in cellular monolayers. *Soft Matter* 11(37):7328–7336.
22. Kaliman S, et al. (2021) Mechanical Regulation of Epithelial Tissue Homeostasis. *Physical Review X* 11(3):031029.
23. Ranft J, et al. (2010) Fluidization of tissues by cell division and apoptosis. *Proceedings of the National Academy of Sciences* 107(49):20863–20868.
24. Basan M, Prost J, Joanny JF, Elgeti J (2011) Dissipative particle dynamics simulations for biological tissues: rheology and competition. *Physical Biology* 8(2):026014.
25. Montel F, et al. (2011) Stress Clamp Experiments on Multicellular Tumor Spheroids. *Physical Review Letters* 107(18):188102.
26. Montel F, et al. (2012) Isotropic stress reduces cell proliferation in tumor spheroids. *New Journal of Physics* 14(5):055008.
27. Puliafito A, et al. (2012) Collective and single cell behavior in epithelial contact inhibition. *Proceedings of the National Academy of Sciences* 109(3):739–744.
28. Zehnder SM, Suaris M, Bellaire MM, Angelini TE (2015) Cell Volume Fluctuations in MDCK Monolayers. *Biophysical Journal* 108(2):247–250.
29. Swaminathan V, Gloerich M (2021) Decoding mechanical cues by molecular mechanotransduction. *Current Opinion in Cell Biology* 72:72–80.
30. Smith JA, Martin L (1973) Do Cells Cycle? *Proceedings of the National Academy of Sciences* 70(4):1263–1267.
31. Sun Y, et al. (2017) Single-cell study of the extracellular matrix effect on cell growth by in situ imaging of gene expression. *Chemical Science* 8(12):8019–8024.
32. Brooks R, Bennett D, Smith J (1980) Mammalian cell cycles need two random transitions. *Cell* 19(2):493–504.
33. Dowling MR, et al. (2014) Stretched cell cycle model for proliferating lymphocytes. *Proceedings of the National Academy of Sciences* 111(17):6377–6382.
34. Podewitz N, Jülicher F, Gompper G, Elgeti J (2016) Interface dynamics of competing tissues. *New Journal of Physics* 18(8):083020.
35. Podewitz N, Delarue M, Elgeti J (2015) Tissue homeostasis: A tensile state. *EPL (Europhysics Letters)* 109(5):58005.
36. Anna-Kristina Marel, Nils Podewitz, Zorn M, Rädler JO, Elgeti J (2014) Alignment of cell division axes in directed epithelial cell migration. *New Journal of Physics* 16(11):115005.
37. Marel AK, et al. (2014) Flow and diffusion in channel-guided cell migration. *Biophysical Journal* 107(5):1054–1064.
38. Büscher T, Diez AL, Gompper G, Elgeti J (2020) Instability and fingering of interfaces in growing tissue. *New Journal of Physics* 22(8).
39. Ganai N, Büscher T, Gompper G, Elgeti J (2019) Mechanics of tissue competition: interfaces stabilize coexistence. *New Journal of Physics* 21(6):063017.
40. Garcia S, et al. (2015) Physics of active jamming during collective cellular motion in a monolayer. *Proceedings of the National Academy of Sciences of the United States of America* 112(50):15314–15319.
41. LeGoff L, Lecuit T (2016) Mechanical Forces and Growth in Animal Tissues. *Cold Spring Harbor Perspectives in Biology* 8(3):a019232.
42. Metzner C, et al. (2018) Pressure-driven collective growth mechanism of planar cell colonies. *Journal of Physics D: Applied Physics* 51(30):304004.
43. Arciero JC, Mi Q, Branca MF, Hackam DJ, Swigon D (2011) Continuum Model of Collective Cell Migration in Wound Healing and Colony Expansion. *Biophysical Journal* 100(3):535–543.
44. Sunyer R, et al. (2016) Collective cell durotaxis emerges from long-range intercellular force transmission. *Science* 353(6304):1157–1161.
45. Dolega ME, et al. (2017) Cell-like pressure sensors reveal increase of mechanical stress towards the core of multicellular spheroids under compression. *Nature Communications* 8(1):14056.
46. Abdul Kafi M, El-Said WA, Kim TH, Choi JW (2012) Cell adhesion, spreading, and proliferation on surface functionalized with RGD nanopillar arrays. *Biomaterials* 33(3):731–739.
47. Seo HR, et al. (2017) Nanopillar Surface Topology Promotes Cardiomyocyte Differentiation through Cofilin-Mediated Cytoskeleton Rearrangement. *ACS Applied Materials & Interfaces* 9(20):16803–16812.
48. Biggs LC, Kim CS, Miroshnikova YA, Wickström SA (2020) Mechanical Forces in the Skin: Roles in Tissue Architecture, Stability, and Function. *Journal of Investigative Dermatology* 140(2):284–290.
49. Samuel MS, et al. (2011) Actomyosin-Mediated Cellular Tension Drives Increased Tissue Stiffness and β-Catenin Activation to Induce Epidermal Hyperplasia and Tumor Growth. *Cancer Cell* 19(6):776–791.
50. Rehfeldt F, et al. (2012) Hyaluronic acid matrices show matrix stiffness in 2D and 3D dictates cytoskeletal order and myosin-II phosphorylation within stem cells. *Integrative Biology* 4(4):422.

DRAFT